



HAL
open science

A thermodynamic motivated RCCM damage interface model in an explicit transient dynamics framework

Paul Larousse, David Dureisseix, Anthony Gravouil, Gabriel Georges

► To cite this version:

Paul Larousse, David Dureisseix, Anthony Gravouil, Gabriel Georges. A thermodynamic motivated RCCM damage interface model in an explicit transient dynamics framework. 7th International Conference on Computational Contact Mechanics (ICCCM 2023), Jul 2023, Torino, Italy. 10.1007/s00466-024-02489-x . hal-04156765

HAL Id: hal-04156765

<https://hal.science/hal-04156765v1>

Submitted on 2 Oct 2024


HAL is a multi-disciplinary open access archive for the deposit and dissemination of scientific research documents, whether they are published or not. The documents may come from teaching and research institutions in France or abroad, or from public or private research centers.

L'archive ouverte pluridisciplinaire **HAL**, est destinée au dépôt et à la diffusion de documents scientifiques de niveau recherche, publiés ou non, émanant des établissements d'enseignement et de recherche français ou étrangers, des laboratoires publics ou privés.



Distributed under a Creative Commons Attribution - NonCommercial 4.0 International License

A thermodynamic motivated RCCM damage interface model in an explicit transient dynamics framework

Paul Larousse^{1,2}  · David Dureisseix¹ · Anthony Gravouil¹ · Gabriel Georges²

Abstract

A framework to solve fast dynamic problems involving a non-smooth interface behavior with contact and decohesion is under concern. In previous works, unilateral contact and impact have been studied in explicit dynamics but no damage nor cohesion were involved. Combining a contact problem and a thermodynamically motivated damage model within the so-called CD-Lagrange explicit dynamics scheme is the aim of this work. To do so, RCCM macroscopic model of adhesion with damage of the interface is studied. The thermodynamic motivation of the model and the use of a symplectic explicit scheme creates a framework based on good energy balance. In this work, illustrations and feasibility are shown for small displacement problems.

Keywords Contact · Impact · Cohesive zone model · Interface · Symplectic scheme · Matrix-free

1 Introduction

Predicting the unmoolding tire process is a motivation for developing numerical simulation tools, and a robust dynamics scheme is mandatory. Indeed, this process leads to fast dynamic events, such as impacts or interface fracture, and implicit schemes exhibit convergence issues and/or possibly high numerical cost, so explicit schemes are of interest. This article therefore focuses on the explicit CD-Lagrange scheme, previously studied for dynamic frictional impacts [1, 2], that provides interesting properties due to its symplectic nature, allowing good conservation properties, among which the discrete energy conservation. The aim is therefore herein to use this scheme as a framework for modeling more complex interface properties in a modular implementation.

Hence the focus is on the behavior of a contact interface between a rigid and a deformable body. To describe it, the Hertz-Signorini and Moreau [2, 3] condition of unilateral contact with a frictional Coulomb's law are used and coupled with a cohesive zone model [4–8] (CZM). The phenomenon of decohesion and adhesion is highlighted as a force required to separate two solids [9]. The Fremond's definition of interface adhesion is the basis of different models [3, 10, 11]. The adhesion is characterised by a parameter β called the “intensity of adhesion”. It is indeed directly related to a damage parameter [12]. The aim of this article is to recast a thermodynamic framework allowing to embed such behavior into a symplectic explicit time integration scheme.

The physical interpretation of damage, especially on an interface, is usually settled at microscopic scale [13–18]. A macroscopic model [3, 10–12, 19, 20] is a phenomenological one, aimed to traduce local behaviors with macroscopic quantities such as a damage parameter [12]. For the present study, a macroscopic model has been chosen to deal with the impact and the damage evolution. The chosen adhesion model is based on a damage parameter taking place as a generalization of the RCCM (Raous–Cangemi–Cocou–Monerie) model [12]. According to the value of this parameter, the stiffness of the interface is modified; the higher is the damage, the lower is the stiffness. Though not tested herein, the adhesion can also be a recoverable phenomenon [21]: the intensity of adhesion can increase or decrease following certain condi-

✉ Paul Larousse
paul.larousse@insa-lyon.fr

David Dureisseix
david.dureisseix@insa-lyon.fr

Anthony Gravouil
anthony.gravouil@insa-lyon.fr

¹ INSA Lyon, CNRS, LaMCoS, UMR5259, 69621
Villeurbanne, France

² Centre de technologie de Ladoux, Manufacture Française de
Pneumatiques Michelin, 63000 Clermont-Ferrand, France

$$\begin{cases} \mathbf{v} &= v_{c,N} \mathbf{n} + v_{c,T} \mathbf{t} \\ \mathbf{r} &= r_{c,N} \mathbf{n} + r_{c,T} \mathbf{t} \\ \mathbf{r}_{c,T} &= r_{c,T} \mathbf{t} \end{cases} \quad (4)$$

with \mathbf{n} computed as the normal vector and \mathbf{t} the tangential direction vector, respectively associated to $v_{c,N}$ and $v_{c,T}$ for the velocity \mathbf{v} and $r_{c,N}$ and $r_{c,T}$ for the impulse \mathbf{r} . In the following, the study will focus on rigid-deformable contact.

The classical formulation involves as state variables at the interface: the normal displacement gap g and the contact forces $\mathbf{F}_{\text{contact}}$. With the previously mention of velocity-impulse formulation, the local contact behavior can be reformulated thanks to Moreau's viability lemma [2, 24, 25] for the normal component as:

$$\begin{cases} \text{if } g > 0, \text{ then } r_{c,N} = 0 \\ \text{else } g = 0, \text{ and } 0 \leq r_{c,N} \perp v_{c,N} \geq 0 \\ \quad (\text{i.e. } r_{c,N} \geq 0, v_{c,N} \geq 0) \\ \quad \text{and } r_{c,N} \cdot v_{c,N} = 0 \end{cases} \quad (5)$$

with $r_{c,N}$ the normal impulse due to contact and $v_{c,N}$ the relative normal velocity between the rigid and deformable bodies. In active contact case ($g = 0$), either the velocity is positive which means there is no impulse anymore because the deformable body is getting away, either there is an impulse, the contact is maintained, so the relative velocity between the two bodies is null.

For the tangential problem one gets [2]:

$$\begin{cases} \text{if } g > 0, \text{ then } r_{c,T} = 0 \\ \text{else } g = 0, \text{ and } \\ \quad 0 \leq (\mu r_{c,N} - r_{c,T}) \perp \|\mathbf{v}_{c,T}\| \geq 0 \\ \quad (\text{i.e. } (\mu r_{c,N} - r_{c,T}) \geq 0) \\ \quad \text{and } (\mu r_{c,N} - r_{c,T}) \cdot \|\mathbf{v}_{c,T}\| = 0 \end{cases} \quad (6)$$

with $r_{c,T} = \|\mathbf{r}_{c,T}\|$ the tangential impulse, $v_{c,T}$ the tangential relative velocity and μ the friction coefficient. There are two different states for the tangential contact. The first one is the sticking state if $\mu r_{c,N} > r_{c,T}$ (no relative velocity between the two bodies). The second one is the sliding state if $\mu r_{c,N} = r_{c,T}$.

Additionally to complete the Coulomb's law one should satisfy to:

$$\mathbf{r}_{c,T} = -a \mathbf{v}_{c,T} \quad (7)$$

with $a \in \mathbb{R}^+$.

With the explicit nature of the CD-Lagrange scheme, the gap is a state variable whose determination is explicit as $\mathbf{g}_{n+1} = \mathbf{L}_N \mathbf{U}_{n+1}$ where \mathbf{L}_N is an operator condensed from the global problem to the normal contact problem for the impulse. \mathbf{L}_T is the corresponding tangential operator. The

dynamical system discretized in time reads:

$$\begin{aligned} \mathbf{M}(\mathbf{V}_{n+3/2} - \mathbf{V}_{n+1/2}) &= h(\mathbf{F}_{\text{ext},n+1} - \mathbf{F}_{\text{int},n+1}) \\ &\quad + \mathbf{L}_N^T \mathbf{R}_{c,N,n+3/2} \\ &\quad + \mathbf{L}_T^T \mathbf{R}_{c,T,n+3/2} \end{aligned} \quad (8)$$

with $\mathbf{R}_c = \mathbf{L}_N^T \mathbf{R}_{c,N} + \mathbf{L}_T^T \mathbf{R}_{c,T}$ the global impulse. When the contact is active, i.e the local gap $g = 0$ Linear Complementary Problems (LCP) (5),(6) have to be solved. Once discretized, it is stated as $g_{n+1} \leq 0$, penetration is accepted. Indeed, since the contact formulation is expressed with the velocity and impulse formulation to address the non-smooth behavior without regularization [24], the constitutive law is satisfied at the velocity level, so this explains why a small penetration appears on the displacement, which is a precision issue, not a stability one [1, 2]. Since local normal and tangential directions are orthogonal, $\mathbf{L}_N \mathbf{L}_T^T = \mathbf{L}_T \mathbf{L}_N^T = \mathbf{0}$; this allows decoupling of local LCPs to be solved. Indeed, the dynamics (2) gives for the global normal part:

$$\begin{aligned} \mathbf{V}_{c,N,n+3/2} &= \mathbf{L}_N \mathbf{V}_{n+3/2} \\ &= \mathbf{V}_{c,N,\text{free}} + \mathbf{H}_N \mathbf{R}_{c,N,n+3/2} \end{aligned} \quad (9)$$

where $\mathbf{V}_{c,N,\text{free}} = \mathbf{L}_N \mathbf{V}_{\text{free}}$ with (3) and $\mathbf{H}_N = \mathbf{L}_N \mathbf{M}^{-1} \mathbf{L}_N^T$ is the so-called Delassus operator which is positive definite operator. With a lumped mass matrix and local contact conditions, this operator is diagonal, leading to an explicit matrix-free solution for $v_{c,N}$ and $r_{c,N}$ once the constitutive behavior (5) is added. The resolution algorithm is detailed in 1. Locally, (9) becomes:

$$v_{c,N,n+3/2} = v_{c,N,\text{free}} + H_{N,\text{loc}} r_{c,N,n+3/2} \quad (10)$$

Once the normal parts are known, the reduced tangential dynamics reads:

$$\begin{aligned} \mathbf{V}_{c,T,n+3/2} &= \mathbf{L}_T \mathbf{V}_{n+3/2} \\ &= \mathbf{V}_{c,T,\text{free}} + \mathbf{H}_T \mathbf{R}_{c,T,n+3/2} \end{aligned} \quad (11)$$

where $\mathbf{V}_{c,T,\text{free}} = \mathbf{L}_T \mathbf{V}_{\text{free}}$ with (3) and $\mathbf{H}_T = \mathbf{L}_T \mathbf{M}^{-1} \mathbf{L}_T^T$ which is also diagonal and positive definite. Locally, (11) becomes:

$$\mathbf{v}_{c,T,n+3/2} = \mathbf{v}_{c,T,\text{free}} + \mathbf{H}_{T,\text{loc}} \mathbf{r}_{c,T,n+3/2} \quad (12)$$

with $\mathbf{H}_{T,\text{loc}}$ the local Delassus operator. Now, by using the local tangential behavior (7) to replace $\mathbf{r}_{c,T}$ in (12), one gets:

$$(\mathbf{1} + \mathbf{H}_{T,\text{loc}} a) \mathbf{v}_{c,T,n+3/2} = \mathbf{v}_{c,T,\text{free}} \quad (13)$$

So $\mathbf{v}_{c,T,\text{free}}$ and $\mathbf{v}_{c,T,n+3/2}$ are parallel vectors, oriented in the same direction. This property allows to derive explicitly

the sliding direction without need for iteration:

$$\mathbf{t} = \frac{\mathbf{v}_{c,T,\text{free}}}{\|\mathbf{v}_{c,T,\text{free}}\|} \quad (14)$$

as a configuration vector. The local tangential LCP therefore has a matrix-free solution as detailed in the algorithm 2.

Algorithm 1 Local impact resolution for normal direction

Input: g_{n+1} , $v_{c,N,\text{free}}$, $H_{N,\text{loc}}$
if $g_{n+1} > 0$ **then**
 $v_{c,N,n+3/2} = v_{c,N,\text{free}}$
 $r_{c,N,n+3/2} = 0$
else
 $v_{c,N,n+3/2} = \langle v_{c,N,\text{free}} \rangle_+$
 $r_{c,N,n+3/2} = -H_{N,\text{loc}}^{-1} \langle v_{c,N,\text{free}} \rangle_-$
end if

Algorithm 2 Local impact resolution for tangential direction

Input: $\mathbf{v}_{c,T,\text{free}}$, $r_{c,N,n+3/2}$, $\mathbf{H}_{T,\text{loc}}$
 $\tilde{\mathbf{r}}_T = -\mathbf{H}_{T,\text{loc}}^{-1} \mathbf{v}_{c,T,\text{free}}$
if $\|\tilde{\mathbf{r}}_T\| \leq \mu r_{c,N,n+3/2}$ **then**
 $\mathbf{r}_{c,T,n+3/2} = \tilde{\mathbf{r}}_T$
 $\mathbf{v}_{c,T,n+3/2} = 0$
else
 $\mathbf{t} = \frac{\mathbf{v}_{c,T,\text{free}}}{\|\mathbf{v}_{c,T,\text{free}}\|}$
 $\mathbf{r}_{c,T,n+3/2} = -\mu r_{c,N,n+3/2} \mathbf{t}$
 $v_{c,T,n+3/2} = \langle \mathbf{v}_{c,T,\text{free}} + \mathbf{H}_{T,\text{loc}} \mathbf{r}_{c,T,n+3/2} \rangle_+$
 $\mathbf{v}_{c,T,n+3/2} = v_{c,T,n+3/2} \mathbf{t}$
end if

In the next paragraph, a first 3D test case is studied using the Finite Element (FE) method. These local algorithms will be used to solve contact problems at each node of the interface.

2.3 Test case 1: compression and shearing of a cube

In order to test this algorithm and especially the explicit nature of the tangential sliding direction, a first test case is proposed. A linear elastic cube is first compressed using a prescribed displacement on the top face against a rigid support, with a frictional contact interaction behavior. Then a lateral pressure is applied on a side face. The aim is to observe the impulse tangential direction evolution. To do so, the FE mesh is generated with the software Cast3M (<http://www-cast3m.cea.fr/>). The test is illustrated in Fig. 1.

The size of the cube is a 10 m by 10 m large, and 8 m high, discretized with $7 \times 7 \times 7$ cubic elements with 8 nodes each, leading to 1536 degrees of freedom. We used a Young Modulus of 10 Pa, a Poisson coefficient $\nu = 0.3$ and a small friction coefficient $\mu = 0.05$. Figure 2 gives the prescribed smooth loading evolutions.

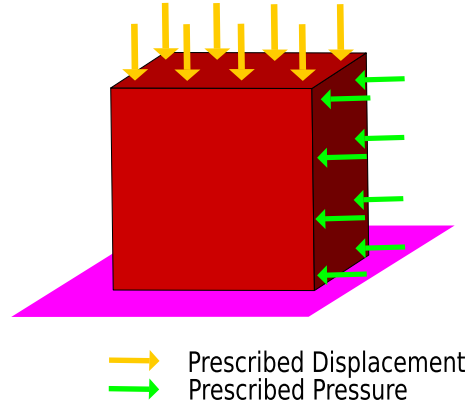


Fig. 1 Test case 1 configuration

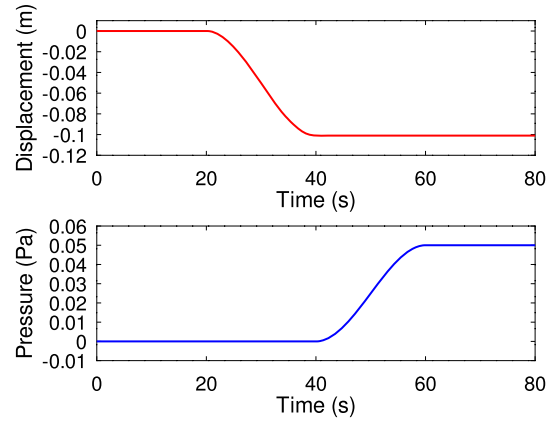


Fig. 2 Prescribed displacement and pressure depending on time

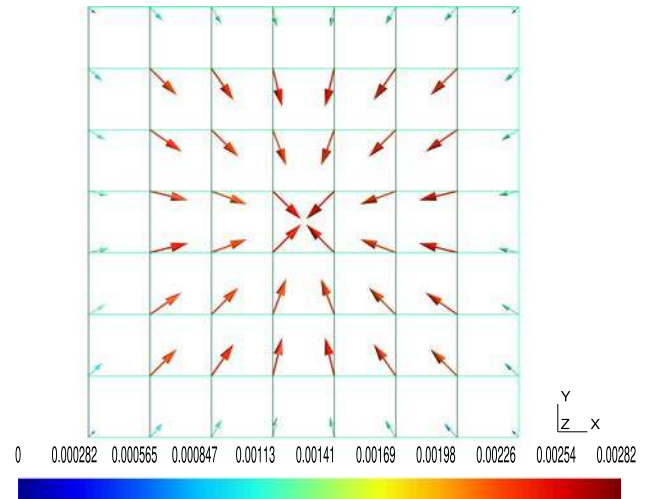


Fig. 3 Tangential impulse ($\text{m s}^{-1} \text{ kg}^{-1}$) direction at $t = 40$ s

During the first loading stage with increasing vertical displacement, the tangential friction directions on the interface are oriented toward the center of the bottom face, as shows Fig. 3, due to Poisson effect. When the pressure is increased on a lateral face of the cube, the tangential friction direction

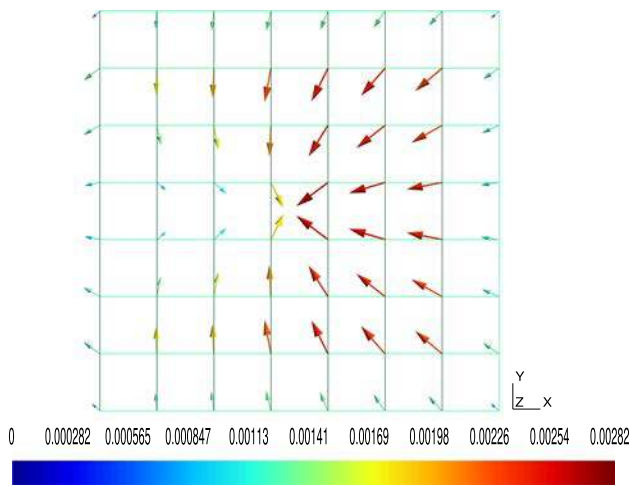


Fig. 4 Tangential impulse ($\text{m s}^{-1} \text{kg}^{-1}$) direction at $t = 45$ s

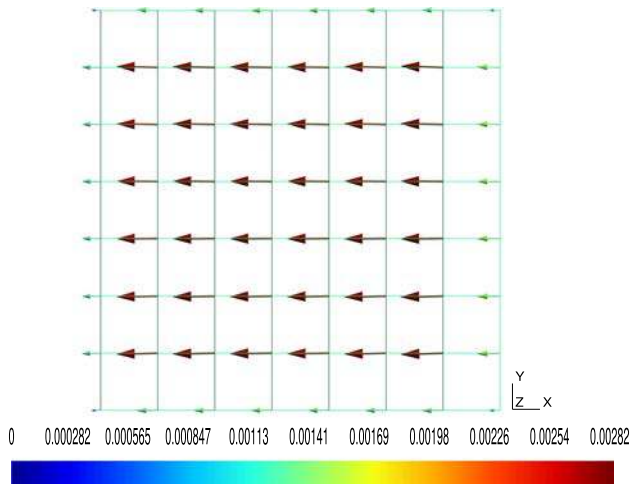


Fig. 5 Tangential impulse ($\text{m s}^{-1} \text{kg}^{-1}$) direction at $t = 50$ s

rotates, as illustrates Fig. 4, and when sliding occurs again, they are aligned with the external forces direction, as shows Fig. 5.

Figure 6 reports that if nothing is applied, then the cube sticks to the ground. In the second part of the simulation with the prescribed displacement, one can observe that there is a lot of increasing and decreasing percentage of sticking interface area. This can be explained by the use of a non-null Poisson coefficient and a really low friction coefficient that leads to a quasi non-existent sticking phase. It is also due to the waves transport which is a dynamical effect due to the choice of an elastic behavior without damping. When the mesh is refined, this phenomenon occurs at the same time as the waves transport velocity is the same. During the prescribed pressure part, one can observe that when the pressure increases, the surface of the cube which is sliding increases. Figure 7 shows the result obtained with a mesh size divided

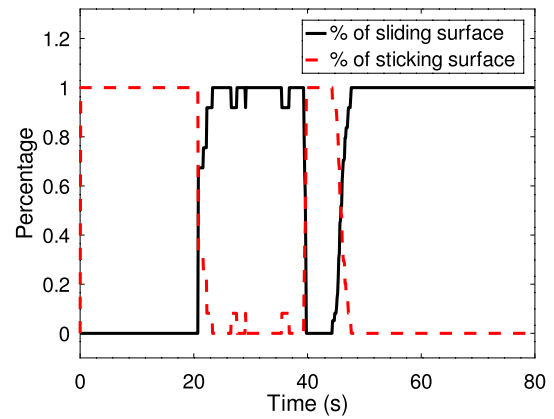


Fig. 6 State area percentages of the interface behavior obtained with the original mesh of $7 \times 7 \times 7$ elements

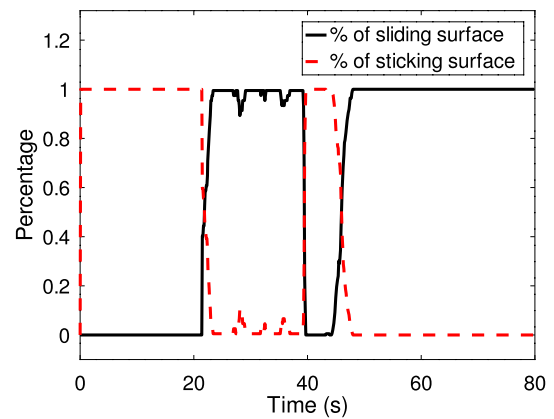


Fig. 7 State area percentages of the interface behavior obtained with the finer mesh of $14 \times 14 \times 14$ elements

by two. The result is slightly dependant from the spatial discretization.

In the next section, a focus is done on the RCCM interface model. The resolution of contact problem is one of the components of this model. A modular thermodynamically based explicit resolution is proposed to solve contact problem with an interface behavior.

3 A cohesive zone model integration

Adhesion phenomenon is a long term study with many definitions [9], from microscopic scale to macroscopic one, depending on the materials involved and the application case, such as composites joints in engineering applications [26] or adhesion with rough surfaces [27] as examples amongst many others. At microscopic scale, many different works [13–18] explain physically what happens. In his works, Christian Talon [3] presents other theories on adhesion phenomenon as the theory of Eley's absorption or the Johnson-Kendall-Roberts adhesion theory [28]. A particular

attention is given to Fremont's definition of adhesion [3, 29] in his studies. Many other cohesive zone models exist [4].

Our study is more concerned with decohesion phenomenon at a macroscopic scale [30]. Previous works [2] studied the contact at this scale with the explicit CD-Lagrange scheme, and the idea herein is to extend the explicit framework to a cohesive zone model, involving interface damage, and preserving the good energetic properties of this explicit scheme using a thermodynamically consistent framework. We focus herein on the RCCM model [11, 12, 20], which has known many updates, and on the unified formulation given by Del Piero-Raous [12]. A first approach with a single degree of freedom model is done in order to validate the model and then an extension is made in 3D.

3.1 RCCM, a thermodynamic motivated model

A thermodynamic motivated model consists in respecting the two first principles of thermodynamics [31]. The RCCM interface model [12] is composed of two parallel parts as shown in the rheology of the simplified single degree of freedom model of Fig. 8. It is composed of a contact part, with normal and tangential behavior as in the previous test case 1, and a damaging elastic interface. Hence, both parts have to verify the thermodynamic framework. Let us define the free energy potential Ψ and a dissipation potential Φ [31] as:

$$\begin{cases} \Psi = \Psi_c + \Psi_d \\ \Phi = \Phi_c + \Phi_d \end{cases} \quad (15)$$

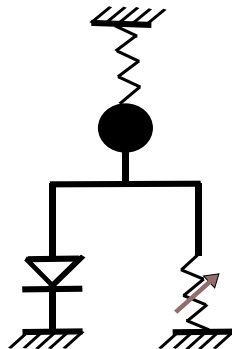
with Ψ_c and Φ_c respectively the free energy and dissipation potentials associated to the contact part behavior, and Ψ_d and Φ_d for the RCCM damaging elastic part. All have to be definite positive and convex.

The following 3D local notations are used:

$$\begin{cases} \mathbf{F}_{contact} = f_{c,N} \mathbf{n} + f_{c,T} \mathbf{t} \\ \mathbf{f}_{c,T} = f_{c,T} \mathbf{t} \end{cases} \quad (16)$$

with \mathbf{n} and \mathbf{t} the normal and tangential vectors respectively.

Fig. 8 Rheology of normal behavior of the RCCM model for the single-dof mass test case



Verifying the principles of thermodynamics means to satisfy the Clausius–Duhem inequality [31] for the model. As the full model is composed of three parts: normal contact, tangential friction and damageable elasticity, each has to verify this inequality.

For the contact part, a free energy potential Ψ_c and a dissipation potential Φ_c are introduced. For normal contact, the state variables are $u_{c,N}$ the normal displacement and $f_{c,N}$ the normal contact force. The state laws [31] read:

$$\begin{aligned} f_{c,N} &\in \partial_{u_{c,N}} \Psi_c(u_{c,N}) \\ \text{or } u_{c,N} &\in \partial_{f_{c,N}} \Psi_c^*(f_{c,N}) \end{aligned} \quad (17)$$

with the sub-differentials of two potentials, Ψ_c^* being the dual of the free energy potential Ψ_c , both defined as:

$$\begin{cases} \Psi_c(u_{c,N}) = \mathbb{I}_{\mathbb{R}^+}(u_{c,N}) \\ \Psi_c^*(f_{c,N}) = \mathbb{I}_{\mathbb{R}^+}(f_{c,N}) \end{cases} \quad (18)$$

which are definite, positive and convex, with $\mathbb{I}_{\mathbb{R}^+}$ the indicator function of the set \mathbb{R}^+ .

Thus the normal contact condition can be written as:

$$u_{c,N} \geq 0 \text{ and } \begin{cases} \text{if } u_{c,N} > 0, & f_{c,N} = 0 \\ \text{if } u_{c,N} = 0, & f_{c,N} \in \mathbb{R}^+ \end{cases} \quad (19)$$

or summarized as:

$$0 \leq u_{c,N} \perp f_{c,N} \geq 0 \quad (20)$$

Using the Moreau's viability lemma [24], these conditions can be written in terms of normal velocity and impulse, as expressed in (5) with g the gap between the two bodies whose interface is studied. In the case of a rigid fixed body, and a deformable body, $g = u_{c,N}$.

Generally speaking, the tangential contact is a non-associated Coulomb's law. Then, a super-potential named bi-potential [32] b is introduced which is a generalization of the potential of dissipation Φ_c and reads $\forall(\mathbf{v}_{c,T}, \mathbf{f}_{c,T}) \in \mathbb{R}^+ \times \mathbb{R}^+$:

$$b(-\mathbf{v}_{c,T}, \mathbf{f}_{c,T}) = \mathbb{I}_{\mathbb{K}_\mu}(\mathbf{f}_{c,T}) + \mathbb{I}_{\mathbb{R}^-}(-\mathbf{v}_{c,T}) + \mu f_{c,N} \|\mathbf{v}_{c,T}\| \quad (21)$$

with $\mathbf{v}_{c,T}$ the tangential relative velocity between two bodies whose interface is studied, $\mathbf{f}_{c,T}$ the tangential contact force, μ the friction coefficient, $f_{c,N}$ the normal contact force and \mathbb{K}_μ the Coulomb's cone:

$$\mathbb{K}_\mu = \{(f_{c,N}, \mathbf{f}_{c,T}), \|\mathbf{f}_{c,T}\| - \mu f_{c,N} \leq 0\} \quad (22)$$

This potential has to be bi-convex and to verify the following property:

$$b(\mathbf{v}_{c,T}, \mathbf{f}_{c,T}) \geq \mathbf{v}_{c,T} \mathbf{f}_{c,T} \quad (23)$$

Now, the constitutive relations read:

$$\begin{aligned} \mathbf{v}_{c,T} &\in \partial_{\mathbf{f}_{c,T}} b(\mathbf{v}_{c,T}, \mathbf{f}_{c,T}) \\ \text{or } \mathbf{f}_{c,T} &\in \partial_{\mathbf{v}_{c,T}} b(\mathbf{v}_{c,T}, \mathbf{f}_{c,T}) \end{aligned} \quad (24)$$

This bi-potential, using (24) allows to recover the classical Coulomb's law [32, 33]:

$$\begin{cases} \text{if } \mathbf{v}_{c,T} = 0, & \|\mathbf{f}_{c,T}\| \leq \mu f_{c,N} \\ \text{else } & \|\mathbf{f}_{c,T}\| = \mu f_{c,N}, \text{ and } \mathbf{f}_{c,T} = -a \mathbf{v}_{c,T} \end{cases} \quad (25)$$

with $a \in \mathbb{R}^+$.

Using the Moreau's viability lemma [24], the tangential contact can be written in term of tangential velocity and impulse, as expressed in (6) with $\mathbf{r}_{c,T} = r_{c,T} \mathbf{t}$, \mathbf{t} the tangential direction defined as in (14). Then, the normal and tangential conditions are included in the thermodynamic framework.

To derive the full RCCM interface model from the thermodynamic framework, the elastic damage part has to be studied. To do so, the Clausius–Duhem inequality is introduced [31]:

$$\mathcal{D} = -\beta \dot{\alpha} \geq 0 \quad (26)$$

with α a damage parameter, $\dot{\alpha}$ the damage rate and β the thermodynamic flux associated to α . The state laws read:

$$\begin{cases} \mathbf{R}_d \in \partial_{[\mathbf{u}]} \Psi_d \\ \beta \in \partial_{\alpha} \Psi_d \end{cases} \quad (27)$$

with \mathbf{R}_d the elastic force distribution (i.e. normal stress), $[\mathbf{u}]$ the relative displacement vector between the surfaces of the two bodies [12] defined as:

$$\begin{cases} [\mathbf{u}]_N = \mathbf{L}_N \mathbf{u} \\ [\mathbf{u}]_T = \mathbf{L}_T \mathbf{u} \end{cases} \quad (28)$$

with \mathbf{u} the displacement vector of the deformable body, \mathbf{L}_N and \mathbf{L}_T the operator presented in Eq. (8) with N and T respectively the normal and tangential notations. Ψ_d is the free energy potential associated to the problem introduced as the convex, definite, positive following potential [12]:

$$\Psi_d([\mathbf{u}], \alpha) = \frac{1}{2} g_N(\alpha) [\mathbf{u}]^2 \quad (29)$$

with g_N the interface stiffness depending on the damage parameter α , for which we select herein the behavior presented in Fig. 9.

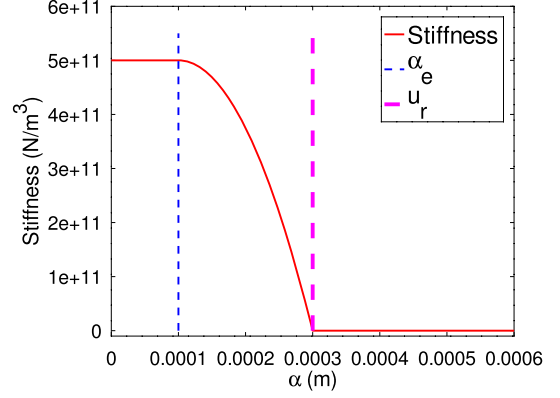


Fig. 9 Interface stiffness evolution

α_e is the elastic limit of the interface, g_e is the initial elastic stiffness of the undamaged interface and u_r the rupture limit of the interface. The stiffness interface behavior is summarized by Eq. (30) as:

$$\begin{cases} \text{if } \alpha < \alpha_e \text{ then } & g_N = g_e \\ \text{else if } \alpha \geq \alpha_e \text{ and } & \alpha < u_r, \\ \text{then } & g_N = g_e \left(1 - \frac{(\alpha - \alpha_e)^2}{(u_r - \alpha_e)^2} \right) \\ \text{else } & g_N = 0 \end{cases} \quad (30)$$

With (27), one gets:

$$\begin{cases} \mathbf{R}_d = g_N(\alpha) [\mathbf{u}] \\ \beta = \frac{1}{2} g'_N(\alpha) [\mathbf{u}]^2 \end{cases} \quad (31)$$

Finally, the evolution of the damage rate $\dot{\alpha}$ needs to be known. The RCCM interface damage model [12] proposes a model with a moving threshold as:

$$\begin{cases} \text{if } f = \alpha \text{ and } & \alpha < u_r, \quad \dot{\alpha} = \langle \dot{f} \rangle_+ \\ \text{else } & \dot{\alpha} = 0 \end{cases} \quad (32)$$

with f the norm of $[\mathbf{u}]$ so \dot{f} is:

$$\dot{f} = \frac{[\mathbf{v}]^t [\mathbf{u}]}{\sqrt{[\mathbf{u}]^t [\mathbf{u}]}} \quad (33)$$

with $[\mathbf{v}]$ the relative velocity between the two bodies which have the studied interface in common. Equation (32) corresponds to the evolution laws which is implicitly derived from the dissipation potential Φ_d introduced in Eq. (15).

By combining (32) and (31), the Clausius–Duhem inequality (26) is verified as soon as g_N is a decreasing function of α , and the RCCM model fits within the thermodynamic framework. The explicit framework presented in the next subsection is based on the thermodynamic one.

3.2 CD-Lagrange framework

To test the RCCM thermodynamic motivated interface model, a single-dof mass test case associated to the rheology model of Fig. 8 is studied. Thus the explicit CD-Lagrange resolution framework is presented in a first hand for a single degree-of-freedom model.

The proposed general scheme design process to solve contact problems with behavior is to express all configuration variables (and so the thermodynamic state laws as well) at time step t_{n+1} . Moreover, rates of variables (and so evolution laws as well) are expressed at half time step $t_{n+3/2}$. This choices are supported by the symplectic aspect of the CD-Lagrange scheme due to his central difference time discretization basis. This emphasizes the explicit computation of configuration. Once discretized, the Eq. (28) and the update of the state variables read:

$$\begin{cases} u_{n+1} = u_n + hv_{n+1/2} \\ [u]_{n+1} = u_{n+1} \\ \alpha_{n+1} = \alpha_n + h\dot{\alpha}_{n+1/2} \end{cases} \quad (34)$$

For the damage rate, the discretized version of (32) is:

$$\begin{cases} \text{if } [u]_{n+1} \geq \alpha_{n+1} \text{ and } \alpha_{n+1} < u_r, \\ \quad \text{then } \dot{\alpha}_{n+3/2} = \langle \dot{f}_{n+3/2} \rangle_+ \\ \text{else } \dot{\alpha}_{n+3/2} = 0 \end{cases} \quad (35)$$

One can notice that this expression is explicit as well, once the configuration (at t_{n+1}) is known.

Finally, the dynamics equation is:

$$\begin{aligned} m(v_{n+3/2} - v_{n+1/2}) = & h(F_{\text{ext},n+1} - F_{\text{int},n+1}) \\ & + r_{c,N,n+3/2} \\ & + hF_{d,N,n+3/2} \end{aligned} \quad (36)$$

The normal direction N is the only direction involved in this test and $r_{c,N,n+3/2}$ is obtained with the algorithm 1.

In order to close the problem, the expression of the damageable elastic interface force F_d in the CD-Lagrange formalism is needed. To do so, the free energy potential relations (31) are used and after time discretization gives:

$$F_{d,N,n+3/2} = sg_N(\alpha_{n+1})[u]_{n+1} \quad (37)$$

with s the supposed contact surface of our single-dof mass. To check how the model evolves, the single-dof mass test case results are presented in the next subsection.

3.3 Test case 2: a single-dof (degree of freedom) mass

The single-dof mass test refers to the rheology model of Fig. 8. The origin of the reference frame is located at the motionless body position. For the test, the chosen parameters are given in Table 1, with m the mass of the single-dof mass, s the contact surface introduced in (37), k the stiffness of the single-dof mass, α_e the elastic limit of the interface, u_r the rupture limit of the interface, h_{CFL} the critical time step [see Eq. (42)] and h the chosen time step.

In order to observe only the elastic damage interface behavior, the stiffness k is null. External force is applied on the single-dof mass. The idea of this test is to check the elastic behavior of the interface by pulling progressively to develop some damage, then to pull strongly in order to go over the rupture threshold u_r and to finally push the single-dof mass on the motionless body to observe the RCCM impact part behavior. To do so, the external force of Fig. 10 is applied. A more classical damage variable [31] $d \in [0, 1]$ can be defined for post-processing step, as:

$$d = 1 - \frac{g_N(\alpha)}{g_N(0)} \quad (38)$$

$d = 0$ denotes no damage and $d = 1$ a fully damaged interface.

With such external force applied, the damage d evolves as in Fig. 11. During the first part of the test when the single-

Table 1 Test case 2 parameters

m (kg)	s (m ²)	k (N/m ³)	α_e (m)
1	1.5×10^{-4}	0	0.0001
u_r (m)	h_{CFL} (s)	h (s)	g_0 (m)
0.0003	0.063	0.001	0

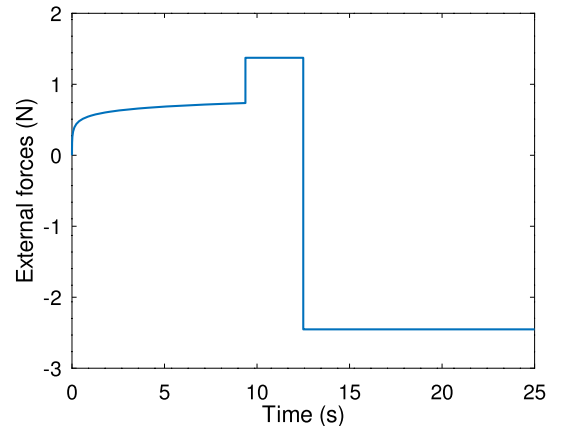


Fig. 10 External force applied on the single-dof mass

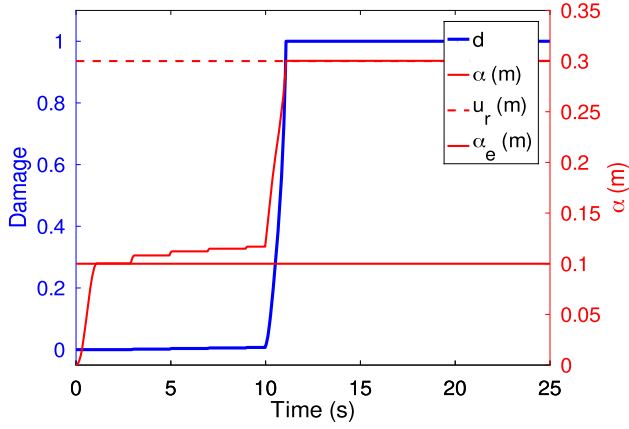


Fig. 11 Damage variable evolution of the single-dof mass

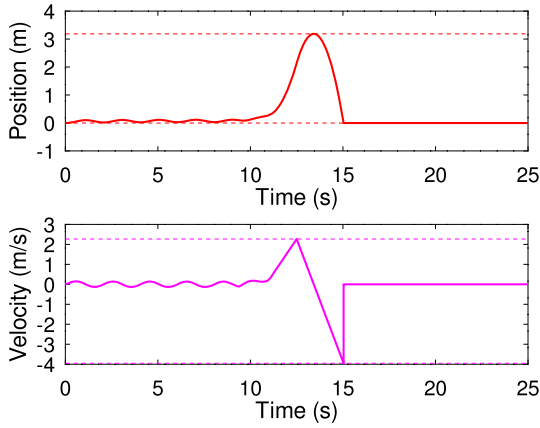


Fig. 12 Position and velocity of the single-dof mass

dof mass is slowly pulled, no damage develops ($d = 0$) till $\alpha = \alpha_e$. Then d and α increase slowly. At time $t = 10$ s, a jump is applied to the force which leads to the interface rupture with $\alpha > u_r$ ($d = 1$). The damage parameter cannot decrease which explains why it is kept constant afterwards. The stepwise evolution of the damage parameter α is due to the velocity oscillations observed on Fig. 12. Indeed it turns to negative periodically and the damage rate is set as the positive value of Eq. (33) which in this case of a single dof is equal to the velocity.

When $\alpha < u_r$, the elastic part of the interface evolves during the damaging process. Oscillations are observed on position and velocity with fast dynamic effects due to the elastic behavior of the interface and vibration of the mass point. At time $t = 10$ s, when rupture happens, the velocity increases as does the position since then the interface stiffness is equal to 0. At time $t = 15$ s, the single-dof mass is strongly pushed on the solid till contact happens thanks to the negative external force. This explains why velocity and position are equal to 0 after this stage. These results can be observed on Fig. 12. One can see that the displacement and the velocity

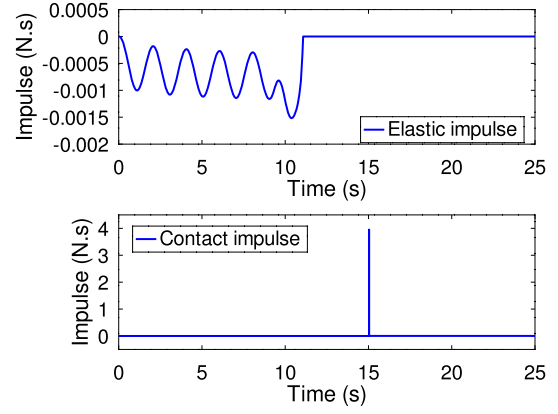


Fig. 13 Impulses on the single-dof mass

oscillate till $t = 10$ s. This behavior is explained by the non smooth beginning of the loading and the elastic behavior without damping of the impulse $hF_{d,N}$ as Fig. 13 shows.

The impulse $hF_{d,N}$ oscillates and reaches a maximum value at interface rupture and then decreases to 0 since then the interface stiffness is zero. For contact impulse, as it is pulled, there is no impulse due to contact. At time $t = 15$ s, when the force is reversed, an impact happens.

To complete this test, the energy balance of the time stepping scheme is studied. It has been proved [1] that the CD-Lagrange scheme is symplectic and has good energetic behavior. The energy balance is given as [1]:

$$\Delta W_{\text{cin},n+1} + \Delta W_{\text{comp},n+1} + \Delta W_{\text{int},n+1} - \Delta W_{\text{ext},n+1} - \Delta W_{IC,n+1} = 0 \quad (39)$$

with in 3D notations:

$$\left\{ \begin{array}{l} \Delta W_{\text{cin},n+1} = \left[\frac{1}{2} \mathbf{V}^T \mathbf{M} \mathbf{V} \right]_n^{n+1} \\ \Delta W_{\text{comp},n+1} = \left[-\frac{1}{8} \mathbf{W}^T \mathbf{M} \mathbf{W} \right]_n^{n+1} \\ \Delta W_{\text{int},n+1} = [\mathbf{U}_n]^T \langle \mathbf{F}_{\text{int},n} \rangle \\ \Delta W_{\text{ext},n+1} = [\mathbf{U}_n]^T \langle \mathbf{F}_{\text{ext},n} \rangle \\ \Delta W_{IC,n+1} = \frac{1}{\Delta t} [\mathbf{U}_n]^T \langle \mathbf{R}_n \rangle \end{array} \right. \quad (40)$$

and the following notations:

$$\left\{ \begin{array}{l} \left[\frac{1}{2} \mathbf{V}^T \mathbf{M} \mathbf{V} \right]_n^{n+1} = \langle \mathbf{V}_n \rangle \mathbf{M} [\mathbf{V}_n] \\ [\mathbf{U}_n] = (\mathbf{U}_{n+1} - \mathbf{U}_n) \\ \langle \mathbf{U}_n \rangle = \frac{1}{2} (\mathbf{U}_{n+1} + \mathbf{U}_n) \\ [\mathbf{V}_n] = \langle \mathbf{W}_n \rangle \\ [\mathbf{U}_n] = \Delta t \langle \mathbf{U}_n \rangle - \frac{\Delta t}{4} [\mathbf{W}_n] \\ \mathbf{W}_{n+1} = \mathbf{V}_{n+3/2} - \mathbf{V}_{n+1/2} \\ \mathbf{R}_{n+1} = \frac{1}{2} (\mathbf{R}_{n+3/2} + \mathbf{R}_{n+1/2}) \\ \mathbf{V}_{n+1} = \frac{1}{2} (\mathbf{V}_{n+3/2} + \mathbf{V}_{n+1/2}) \end{array} \right. \quad (41)$$

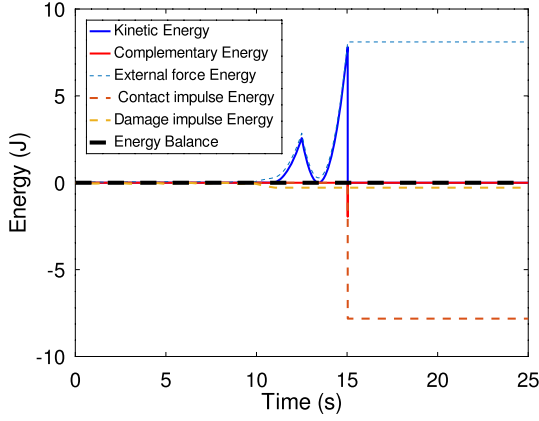


Fig. 14 Energy balance

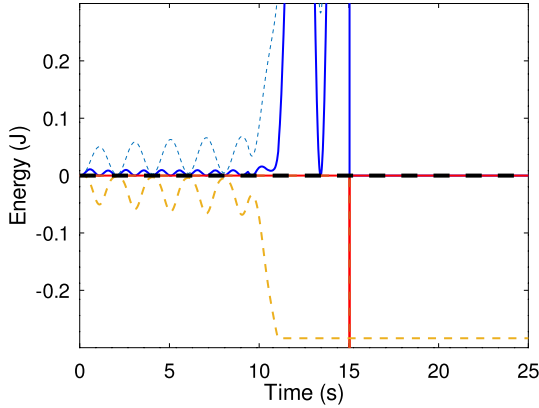


Fig. 15 Figure 14 energy balance zoom

with $\mathbf{R} = \mathbf{R}_c + h\mathbf{F}_d$. As the work is done on a single-dof mass with one degree of freedom, all variables are scalars. $\Delta W_{\text{cin},n+1}$ is the kinetic energy, $\Delta W_{\text{comp},n+1}$ is a numerical complementary energy due to the non regularity of the velocity, $\Delta W_{\text{int},n+1}$ is the work of internal forces which will be null in this test case because a stiffness k of value 0 is chosen, $\Delta W_{\text{ext},n+1}$ is the work of external force (Fig. 10) and $\Delta W_{IC,n+1}$ is the work of the impulses.

Figures 14 and 15 give the results in terms of energies on this test case. At each time step, the cumulative work is computed with the previous time step works. The energy balance (Eq. 39) is respected. Till time $t = 10$ s, a low loss of damage impulse work energy can be observed with a jump when the rupture occurs. The oscillations are due to the elastic behavior of the interface. This is compensated by the external force work and the kinetic energy. At time $t = 15$ s, a big loss of energy is observed due to the contact impulse work. The kinetic energy is transferred to the contact impulse energy loss. At impact, a spike is observed on the complementary energy due to the velocity reaching 0 instantaneously at impact.

The aim of this single-dof mass test case was to validate the model. In the next section, a 3D study is realized.

4 A 3D extension: test case validation

An explicit time integration implies a critical time step h_{CFL} for the numerical stability. In order to obtain it, the following formulation has been used [34, 35]:

$$h_{\text{CFL}} = \frac{2}{w_{\text{max}}} \quad (42)$$

with w_{max} the largest eigenfrequency of the structure. In the case of a problem with an elastic linear material without interface, it is given by [34]:

$$w_{\text{max}} = \sqrt{4 \frac{k}{m}} \quad (43)$$

with m the mass of the system and k the stiffness of the deformable body such as:

$$\begin{cases} k = \frac{Es}{l_c} \\ m = \rho s l_c \end{cases} \quad (44)$$

ρ is the density of the deformable body, E is the Young Modulus of the deformable body, l_c a characteristic length linked to the radius of the inscribed sphere in a mesh element and s an area linked to this characteristic length. In the case of cubic elements, $s = l_c^2$. In order to take into account the interface stiffness k_i , the formulation herein used for the largest eigenfrequency of the structure is the Eq. (45) [34].

$$w_{\text{max}} = \sqrt{\frac{k}{m} \left[2 + \frac{k_i}{k} + \sqrt{4 + \left(\frac{k_i}{k}\right)^2} \right]} \quad (45)$$

with

$$k_i = s \max_{\alpha} (g_N(\alpha)) \quad (46)$$

with g_N the interface stiffness presented on Fig.9. Thus when an interface steps in, the critical time step decreases. Therefore, when damage is added, the interface stiffness will decrease, and so w_{max} will decrease (45) and by consequence the critical time step h_{CFL} will increase as shows Eq. (42). Therefore it is necessary to take a time step h lower than the one computed with the undamaged interface. Also, the eigenfrequency used to compute the critical time step should be the maximum between Eqs. (43) and (45). To avoid the interface impact on the critical time step, methods, that are not applied here, as the selective mass scaling can be used

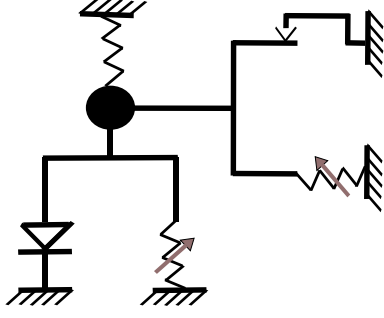


Fig. 16 3D rheology model

[36, 37]. The critical time steps for the following 3D test cases were computed experimentally, based on Eq. (45) as it gives us a lower bound.

4.1 A 3D generalization

A first step to 3D generalization consists in taking into account all directions of displacement. The rheology model presented in Fig. 16 illustrates this. The bottom part of the model concerns the normal direction and the upper right part the tangential one. One can observe that each part involves an elastic damage behavior. The normal direction involves an unilateral normal contact and the tangential direction a friction pad, associated to the friction coefficient μ of the Coulomb's law which depends on the damage parameter α in this model (47) in a mixture law form (between micro cracked and micro elastic partial areas of the elementary interface surface). On the normal direction, one can observe an identical behavior as in the single point mass case. The behavior of the tangential contact is associated with a Coulomb's law [2]. The same damage interface behavior is chosen for each direction, meaning that it is the same interface stiffness behavior according to α (Fig. 9). The damage parameter α is common for each direction, so $g_T = g_N$ with g_T and g_N respectively the tangential and normal interface stiffness. The friction coefficient is:

$$\mu(\alpha) = \mu_{\text{inf}} \left(1 - \frac{g_N(\alpha)}{g_N(0)} \right) \quad (47)$$

where μ_{inf} is the friction value when the interface is no more cohesive. If the interface damage increases, then the friction effect increases too.

Finally, an extension to the evolution law (35) to the 3D cases is required. A generalization of the norm of the relative displacement between the two solids in the function f is generalized as:

$$f([\mathbf{u}]) = \sqrt{[\mathbf{u}]_N + \lambda[\mathbf{u}]_T} \quad (48)$$

with λ a parameter allowing to weight the influence of the tangential behavior, $[\mathbf{u}]_N$ and $[\mathbf{u}]_T$ respectively the normal and tangential values of the relative displacement $[\mathbf{u}]$.

The evolution law (35) becomes (49):

$$\begin{cases} \text{if } f([\mathbf{u}]_{n+1}) \geq \alpha_{n+1} \text{ and } \alpha_{n+1} < u_r, \\ \text{then } \dot{\alpha}_{n+3/2} = < \dot{f}_{n+3/2} > + \\ \text{else } \dot{\alpha}_{n+3/2} = 0 \end{cases} \quad (49)$$

The elastic damage interface force distribution \mathbf{R}_d has components in each local direction. At each FE node of the interface they read:

$$\begin{cases} R_{d,N,n+1} = g_N(\alpha_{n+1}) \mathbf{L}_N \mathbf{u}_{n+1} \\ R_{d,T,n+1} = g_T(\alpha_{n+1}) \mathbf{L}_T \mathbf{u}_{n+1} \end{cases} \quad (50)$$

where \mathbf{L}_N and \mathbf{L}_T are the same local generators as in (8). Using finite elements, the integration of the interface quantities is also an interesting feature. Herein, to comply with the nodal contact formulation, we wish to maintain a consistent description of the other interface quantities. We therefore select to define them at the interface nodes, and so, need for a nodal integration. A classical interpretation is the use of the mass-like boundary matrix (cross-product of interfacial shape functions) to map a force distribution to nodal generalized forces; this approach is nevertheless only valid for low-order finite elements, as will be used herein. Lumping this mass-like matrix corresponds to defining nodal weights that may serve for local integration. An other, more suited approach, is to compute the generalized forces associated to a uniform unitary pressure on the interface. The orientations of these forces are the integrated normal directions at each interface node, and their amplitudes are exactly the previous nodal weights for integration. Then the generalized damage impulse is given by Eq. (51) where \mathbf{S} is a diagonal matrix of nodal weights. Hence the elastic damage interface force reads:

$$\mathbf{F}_{d,n+3/2} = \mathbf{S} (\mathbf{L}_N^T \mathbf{R}_{d,N,n+1} + \mathbf{L}_T^T \mathbf{R}_{d,T,n+1}) \quad (51)$$

It is important to remark that the damage parameter α is independent on each node. Then in 3D the new mechanical equation to solve is:

$$\begin{aligned} \mathbf{M}(\mathbf{V}_{n+3/2} - \mathbf{V}_{n+1/2}) &= h(\mathbf{F}_{\text{ext},n+1} - \mathbf{F}_{\text{int},n+1}) \\ &\quad + \mathbf{L}_N^T \mathbf{R}_{c,N,n+3/2} \\ &\quad + \mathbf{L}_T^T \mathbf{R}_{c,T,n+3/2} \\ &\quad + h \mathbf{F}_{d,n+3/2} \end{aligned} \quad (52)$$

Hence the velocity without contact \mathbf{V}_{free} introduced in (3) becomes:

$$\mathbf{V}_{\text{free}} = \mathbf{V}_{n+1/2} + h \mathbf{M}^{-1} (\mathbf{F}_{\text{ext},n+1} - \mathbf{F}_{\text{int},n+1}) + h \mathbf{M}^{-1} \mathbf{F}_{d,n+3/2} \quad (53)$$

The overall algorithm for the time stepping increment of the resolution is depicted in Algorithm 3. It deals with an interface with a partly smooth behavior (cohesive model) and partly non-smooth (impact with friction), with rigid-deformable model with small displacement assumption.

Algorithm 3 Time increment resolution steps

- Inputs:** $\mathbf{V}_{n+1/2}, \mathbf{U}_n, \alpha_n, \dot{\alpha}_{n+1/2}$
1. Explicit configuration computation: get $\mathbf{U}_{n+1}, \mathbf{g}_{n+1}, [\mathbf{u}]_{n+1}, \alpha_{n+1}$ with (34)
 2. Explicit smooth state laws:
 - Get $\mathbf{F}_{\text{int},n+1}$ with the chosen law for the deformable body
 - Get $\mathbf{R}_{d,n+1}$ with (50)
 3. Matrix-free dynamics:
 - Compute $\mathbf{F}_{d,n+3/2}$ with (51)
 - Compute \mathbf{V}_{free} with (53)
 - Explicit solve of local LCPs with algorithms 1 and 2 to get $\mathbf{R}_{e,n+3/2}$
 - Matrix-free full dynamics solve of (52) to get $\mathbf{V}_{n+3/2}$
 4. Local matrix-free evolution laws (49) to get $\dot{\alpha}_{n+3/2}$
- Outputs:** $\mathbf{V}_{n+3/2}, \mathbf{U}_{n+1}, \alpha_{n+1}, \dot{\alpha}_{n+3/2}$
-

One can notice that getting $\dot{\alpha}_{n+3/2}$ depending on $\dot{f}_{n+3/2}$ (49) depending itself on $\mathbf{V}_{n+3/2}$ (33) is explicit because the dynamics is solved before the evolution of the damage rate [see algorithm (3)].

The advantages of a such proposed framework is that a good energy balance is ensured, and it is modular. In fact, thanks to the explicit matrix-free resolution, the configuration is known. Hence the internal forces can be easily modified by a thermodynamic admissible material behavior as for the interface behavior. The RCCM interface behavior is taken in this article as example.

4.2 Test case 3a: cube RCCM

As first test case in 3D, a cube with an RCCM interface behavior on its bottom face with a motionless body is studied. The test is depicted in Fig. 17.

It is a rigid-deformable interaction, so only the cube is meshed with finite elements. In order to observe the interface

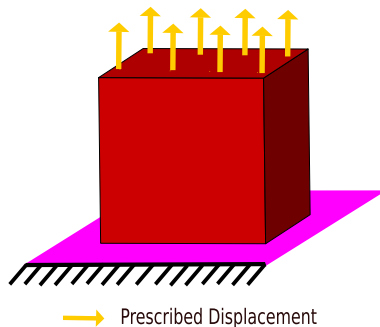


Fig. 17 Test case: cube with RCCM interface

Table 2 Test case 3a parameters

E (Pa)	ν	ρ (kg/m ³)	μ_{inf}	α_e (m)
10^8	0.3	1000	0	0.0001
u_r (m)	h_{CFL} (s)	h (s)	λ	g_0 (m)
0.0003	2.34×10^{-5}	1×10^{-5}	1	-1×10^{-16}

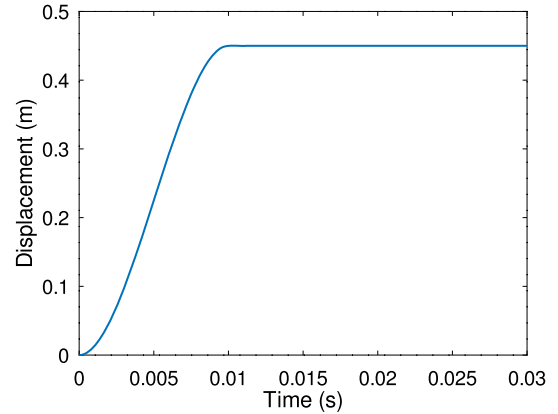


Fig. 18 Prescribed displacement evolution on the cube top face

behavior, an imposed displacement is applied on the top face in order to pull the cube off the motionless body. The idea is to slowly break the interface and to observe each node behavior. The structure is a 1 m \times 1 m \times 1 m cube and is meshed with of 343 eight-nodes cubic elements and 512 nodes. The parameters chosen for this test are summarized in Table 2.

The chosen Young modulus E is close to the one of a rubber elastomer. Poisson's effect is taken into account and there is no friction. For the interface stiffness, the behavior shown on Fig. 9 is chosen. In this test, there is no damping, which means that dynamic effects are observed during all time interval in the final results: elastic waves are propagating in the deformable body leading to long term oscillations. The prescribed vertical displacement on the nodes of the top face of the cube is given on Fig. 18. Nothing is prescribed on the other directions.

In the first 0.01 s of simulation, the displacement increases regularly. However some get the same damage evolution, for example on the edges of the interface surface. In the rest of the simulation the idea is to observe what happens after decohesion. As the material is really elastic, the cube adopts a spring behavior. Figure 19 shows that the final damage parameter value for each node is sometimes much higher than u_r . This is explained by the damaging rate which increases to infinite when the time step h tends to zero. Physically speaking, it is of interest to introduce a limited damage rate. This will be detailed on another damage rate model in Sect. 5.

In order to observe the evolution of the interface damage, percentages of the interface in three different states are shown

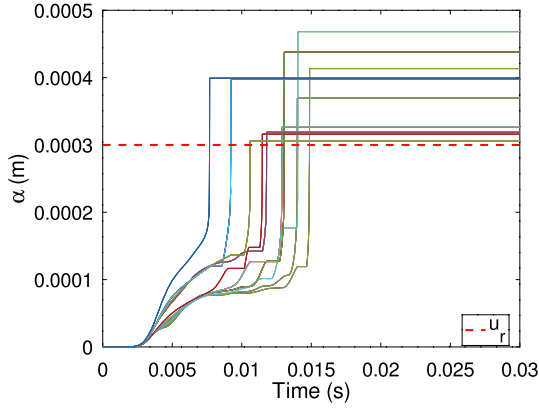


Fig. 19 Damage variable evolution for each nodes

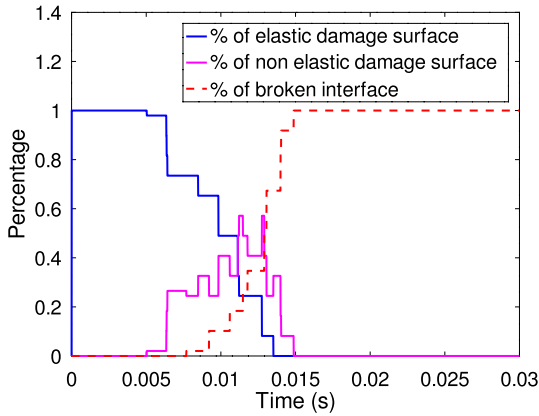


Fig. 20 Percentage of surface states

on Fig. 20. The first one is the percentage of interface area in an elastic state (i.e. $\alpha < \alpha_e$), the second one is the percentage of area partially damaged (i.e. $\alpha_e \leq \alpha < u_r$). The third curve is the percentage of cracked area (i.e. $\alpha > u_r$).

During the first part of the loading evolution, when the displacement imposed on the top face cube increases, all interface nodes are in an elastic state, then every node goes to broken state till every node is broken. In this test $\mathbf{r}_{c,N} = \mathbf{r}_{c,T} = 0$ for every nodes at every time as the interface is only pulled.

In order to validate the results, the resolution of this problem was implemented in the FE software MEF++ developed by the GIREF (Groupe Interdisciplinaire de Recherche en Éléments Finis, <https://giref.ulaval.ca/>) at the University of Laval in Canada and designed to solve industrial applications with a large number of degrees of freedom. To realize the Test case 3a, the same parameters of Table 2 are used, only the initial gap is modified to $g_0 = -1 \times 10^{-10}$ due to contact detection tolerance in MEF++.

To compare the results between both codes, the following relative error is used.

$$Error = \frac{\|\tilde{\mathbf{U}}_{z,MEF++} - \tilde{\mathbf{U}}_{z,Matlab}\|_2}{\|\tilde{\mathbf{U}}_{z,Matlab}\|_2} = 0.0018 \quad (54)$$

using the 2-norm $\|\cdot\|_2$, with $\tilde{\mathbf{U}}_{z,MEF++}$ the values of the mean interface displacement in the direction of pulling at each time step obtained with MEF++, and $\tilde{\mathbf{U}}_{z,Matlab}$ the one obtained with Matlab. An error of only 0.18 % is observed which can be explained by the different optimization algorithms used to solve FE problems in each code and the use of differently sized computers, as the calculus on MEF++ is not realized with the same one used for Matlab. Also, in previous works, the CD-Lagrange scheme was compared with other ones using test cases without the damage law for the interface [38].

Now, the focus is on the control of the damage rate. To do so, we propose to introduce a delayed damage model.

5 An explicit delayed damage model

Damage evolutions often lead to physical and/or numerical difficulties, such as damage localisation, dependence on discretization preventing convergence... Different model modifications to solve these issues have been proposed, such as localization limiters [39, 40]. These approaches are less efficient in dynamics and prevent the explicit nature of the problem. Therefore, another approach, the so-called delayed damage [22, 41].

Here, we propose to extend the previous RCCM interface model to delayed damage in order to limit the damage rate. Moreover, the idea of this section is to use another interface behavior model that verify the thermodynamic in order to use the proposed explicit framework.

5.1 RCCM delayed damage model

To provide the RCCM delayed damage interface model, the normal contact behavior (5) and the tangential friction behavior (6) are conserved. Thanks to the proposed framework, the implementation is trivial, and the only modification is the explicit computation of the damage rate. To control it, the only modification of the previous RCCM interface model (see Sect. 3) relies on the update of the damage rate (32). Based on previous research [22], the following delayed damage rate is studied (55):

$$\begin{cases} \text{if } f(\mathbf{u}) = \alpha \text{ and } \alpha < u_r, \\ \dot{\alpha} = v_r \left[1 - \exp\left(-\frac{1}{v_r} \langle \dot{f} \rangle_+\right) \right] \\ \text{else } \dot{\alpha} = 0 \end{cases} \quad (55)$$

This model is an extension of the previous RCCM interface model [12]. v_r is an additional parameter interpreted as the maximum value of damage parameter rate, since one gets $0 \leq \dot{\alpha} \leq v_r$. Moreover, if $v_r \rightarrow +\infty$, the previous RCCM model is recovered.

As for the previous RCCM interface model studied, this last model complies with the thermodynamic framework as well {since $\dot{\alpha} \geq 0$ and $\dot{g}_N(\alpha) \leq 0$, leading to $-\beta\dot{\alpha} \geq 0$ [Eq. (26)]}.

The discretized version of (55) in the explicit CD Lagrange framework reads:

$$\begin{cases} \text{if } f([\mathbf{u}]_{n+1}) \geq \alpha_{n+1} \text{ and } \alpha_{n+1} < u_r, \\ \dot{\alpha}_{n+3/2} = v_r \left[1 - \exp\left(-\frac{1}{v_r} \langle \dot{f}_{n+3/2} \rangle_+\right) \right] \\ \text{else } \dot{\alpha}_{n+3/2} = 0 \end{cases} \quad (56)$$

Tough $\dot{f}_{n+3/2}$ is involved, the explicit character is kept, since the dynamic evolution is solved before the evolution laws, therefore provided $\mathbf{v}_{n+3/2}$, so $\dot{f}_{n+3/2}$ with (33). To compare the results with the RCCM damage interface model, the test case 3a (Fig. 17) with the same parameters of Table 2 is studied with this new model.

5.2 Test case 3b: delayed damage cube RCCM

The previous test case 3a was a cube with an RCCM interface on its bottom face. On its top face, a displacement is progressively applied (see Fig. 18) in order to peel the whole interface and break it. The present test 3b uses the delayed RCCM interface model presented in the previous subsection instead of the standard one applied for the test 3a. The aim is to slow down the peeling by applying a limit damage velocity v_r . For the test, a maximum damage rate of $v_r = 0.4 \text{ m.s}^{-1}$ is selected.

Figure 21 shows that the interface is fully damaged on all the nodes. This results are obtained with the same test

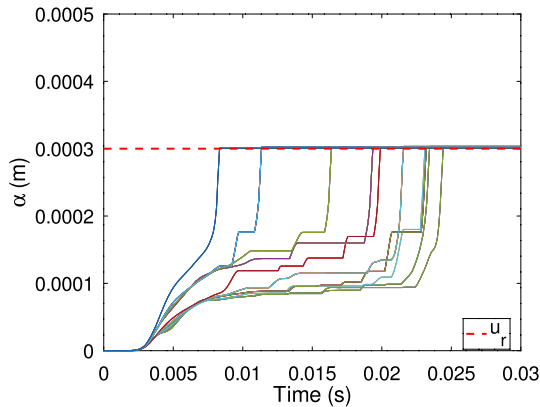


Fig. 21 Damage variable evolution for each node with delayed effect (right)

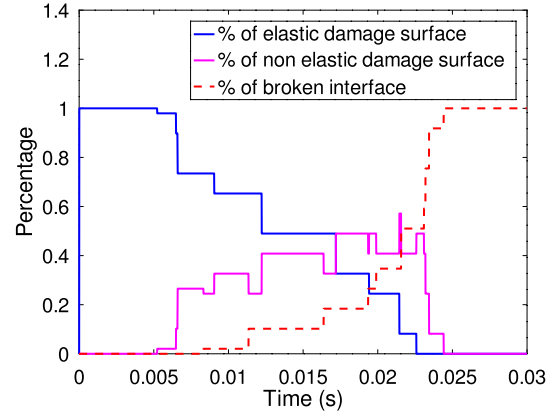


Fig. 22 Percentage of surface states with the interface RCCM delayed damage effect model

case configuration of the test case 3a whose results in terms of interface damage variable evolution are shown in Fig. 19. The curves of α evolution for each node of the interface are more regular (Fig. 21) than the one with no delay (Fig. 19). With this limitation the velocity can not go to infinite. An asymptotic behavior is obtained, all α of each nodes tends to u_r , the rupture limit of interface.

As for the damage variable evolution between both models, the percentage of surface states can also be compared. Figure 22 shows the result obtained with the delayed damage effect as Fig. 20 shows the results obtained with the interface RCCM Standard model. Whereas at half time the whole interface is broken with the standard RCCM, with the delayed one, broken state evolution is more progressive. The interesting effects of the delayed RCCM interface model are highlighted.

The maximum damage rate v_r could be considered as a physical parameter associated to the used materials itself. Once the parameter determined, the delayed damage RCCM interface model should give results closer to the reality and then give better simulations.

5.3 Test case 4: peeling

To conclude on 3D tests, the RCCM interface delayed model is applied on more complex case: the peeling problem. A pressure is applied on a side of a rectangular solid. The interface between this solid and the ground is studied. The idea is to peel the interface gradually. The scheme of the test is presented in Fig. 23. As in the previous test, the Young Modulus of the rectangle is $E = 10^8 \text{ Pa}$ and the Poisson's coefficient $\nu = 0.3$ and still no friction. The time step chosen is $h = 1 \times 10^{-5} \text{ s}$ for a $h_{\text{CFL}} = 2.34 \times 10^{-5}$.

The applied pressure is a parabolic distribution on the side rectangular face. The value on top and bottom edges of the rectangular side under pressure is null, while Fig. 24 depicts the time evolution of the pressure at the mid height, i.e. the

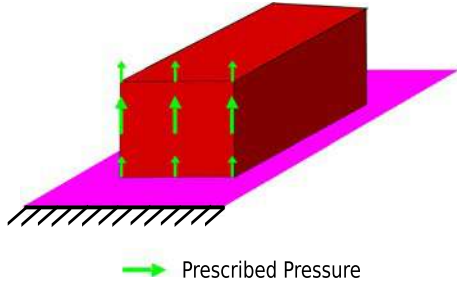


Fig. 23 Peeling test configuration

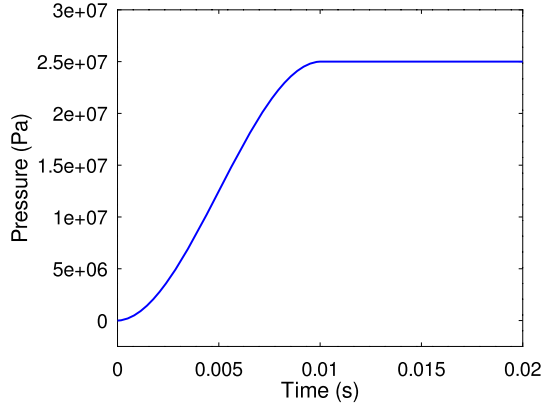


Fig. 24 Peeling test prescribed pressure

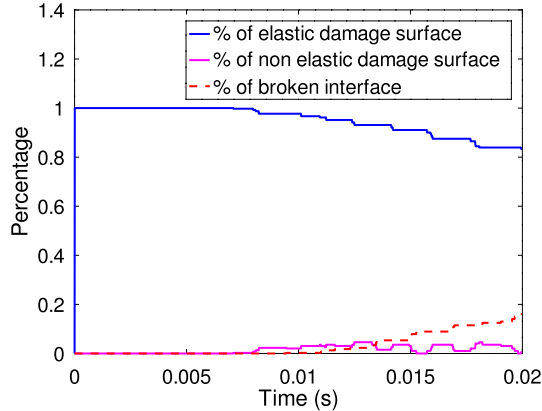


Fig. 25 Percentages of surface state for peeling test

maximum pressure. Then an interpolation is applied in order to obtain a parabolic distribution on the side.

To avoid numerical round-off, the initial gap g_0 is set as in Table 2. As in the previous test, percentages of different states of each node are studied. As the pressure increases, the stress becomes stronger on the interface on the pressured face. When stresses are high enough, the damage parameter increases up to the rupture limit u_r . At that point the interface stiffness nullifies. Figure 25 shows that at half time of the test, the interface starts to break. As the pressure over the side rectangle face increases and stabilizes, the number of nodes of the broken interface increases till the end of the test.

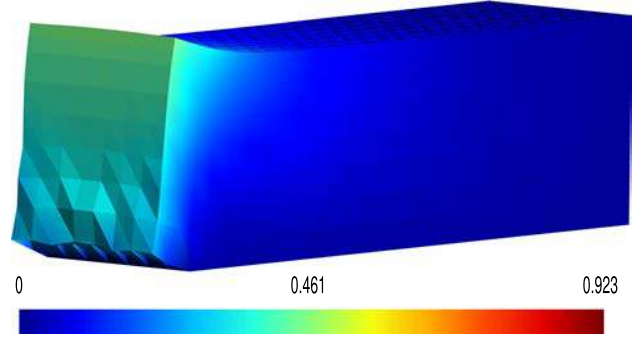


Fig. 26 Mesh displacement (m) during Peeling test

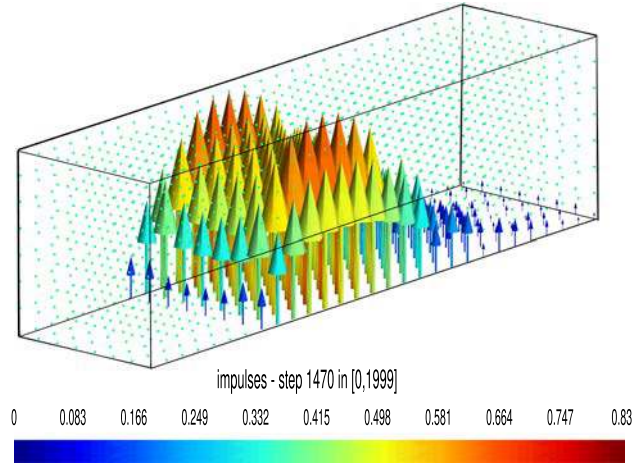


Fig. 27 Contact impulses ($\text{m s}^{-1} \text{kg}^{-1}$) during peeling test

The rotation of the rectangle top face due to peeling as shown in Fig. 26 leads to a compressive contact reaction force on the interface, and so to a contact impulse as depicted on Fig. 27.

Figures 26 and 27 illustrate the deformed mesh during the peeling test and the contact impulses due to peeling at $t = 0.0147 \text{ s}$.

6 Conclusion and perspectives

In this article, a framework for solving non-smooth transient dynamics problems together with contact, damage, decohesion, adhesion in cohesive zone models is presented and illustrated with several test cases. The design framework is composed of two main ingredients. The first one is the use of an explicit dynamics scheme, the so-called CD-Lagrange, that allows to manage unilateral contact and tangential frictional contact. The second one is the thermodynamic motivation of the model. Indeed, it has to respect the first two principles of thermodynamics to be solved. To do so the RCCM damage interface model has been chosen. A first study is made for a single-dof model in order to illustrate

the model behavior and exemplifying the thermodynamic motivation for designing such a scheme. An extension to 3D test cases is made in a consistent way, using the proposed framework. The interest is also to enable the integration of other models within the same framework with ease, both for the scheme design and the implementation. This is also illustrated with the embedding of a delayed damage feature, allowing to overcome some previous limitations of the model, and still suited to a matrix-free parallel architecture of the code. The good energy preserving properties of the scheme also allows to compute the physical dissipation of the model, without blurring the energy balance with numerical artificial dissipation.

To complete this work, a study of the physical meaning of the limit damage rate v_r in the delayed RCCM interface model would be interesting, especially from a possible inverse identification from experiments. Furthermore, other interface models can be tested within the same framework, still valid for many non-linear and even non-smooth behaviors. Moreover an adaptation of the resolution to large transformation mechanical problems is of interest also in the body of the structure, involving other kinds of non-linearities that on the interface between bodies.

Acknowledgements We gratefully acknowledge the French National Association for Research and Technology (ANRT, CIFRE Grant No. 2021/0957). This work was supported by the “Manufacture Française de Pneumatiques Michelin”.

Declarations

Conflict of interest The authors declare that they have no conflict of interest.

References

- Fekak F-E, Brun M, Gravouil A, Depale B (2017) A new heterogeneous asynchronous explicit-implicit time integrator for nonsmooth dynamics. *Comput Mech* 60:1–21. <https://doi.org/10.1007/s00466-017-1397-0>
- Di Stasio J (2021) The CD Lagrange scheme, a robust explicit time-integrator for impact dynamics : a new singular mass formulation, and an extension to deformable-deformable contact. Ph.D. Thesis, INSA, Lyon
- Talon C, Curnier A (2003) A model of adhesion coupled to contact and friction. *Eur J Mech - A/Solids* 22:545–565. [https://doi.org/10.1016/S0997-7538\(03\)00046-9](https://doi.org/10.1016/S0997-7538(03)00046-9)
- Chiaruttini V, Geoffroy D, Riolo V, Bonnet M (2012) An adaptive algorithm for cohesive zone model and arbitrary crack propagation. *Eur J Comput Mech* 21(3–6):208–218. <https://doi.org/10.1080/17797179.2012.744544>
- Pundir M, Anciaux G (2021) Coupling between cohesive element method and node-to-segment contact algorithm: implementation and application. *Int J Numer Methods Eng* 122(16):4333–4353. <https://doi.org/10.1002/nme.6705>
- Eghbalpoor R, Akhavan-Safar A, Jalali S, Ayatollahi MR, Da Silva LFM (2023) A progressive damage model to predict the shear and mixed-mode low-cycle impact fatigue life of adhesive joints using cohesive elements. *Finite Elements Anal Des*. <https://doi.org/10.1016/j.finel.2022.103894>
- Alfano G, Sacco E (2006) Combining interface damage and friction in a cohesive-zone model. *Int J Numer Methods Eng* 68:542–582. <https://doi.org/10.1002/nme.1728>
- Collins-Craft NA, Bourrier FVA (2022) On the formulation and implementation of extrinsic cohesive zone models with contact. *Comput Methods Appl Mech Eng*. <https://doi.org/10.1016/j.cma.2022.115545>
- Kendall K (1971) The adhesion and surface energy of elastic solids. *J Phys D Appl Phys* 4(8):1186–1195. <https://doi.org/10.1088/0022-3727/4/8/320>
- Raous M, Cangémi L, Cocu M (1999) A consistent model coupling adhesion, friction, and unilateral contact. *Comput Methods Appl Mech Eng* 177(3–4):383–399. [https://doi.org/10.1016/s0045-7825\(98\)00389-2](https://doi.org/10.1016/s0045-7825(98)00389-2)
- Raous M, Monerie Y (2002) Unilateral contact, friction and adhesion: 3D cracks in composite materials. In: Martins JAC, Marques MDPM (eds) *Contact mechanics. Solid mechanics and its applications book series*, vol 103. pp 333–346. https://doi.org/10.1007/978-94-017-1154-8_36
- Del Piero G, Raous M (2010) A unified model for adhesive interfaces with damage, viscosity, and friction. *Eur J Mech A Solids* 29(4):496–507. <https://doi.org/10.1016/j.euromechsol.2010.02.004>
- Brink T, Molinari J-F (2019) Adhesive wear mechanisms in the presence of weak interfaces: insights from an amorphous model system. *Phys Rev Mater* 3:053604. <https://doi.org/10.1103/PhysRevMaterials.3.053604>. arXiv:1901.07466 [cond-mat.mtrl-sci]
- Dimaki AV, Shilko EV, Dudkin IV, Psakhie SG, Popov VL (2020) Role of adhesion stress in controlling transition between plastic, grinding and breakaway regimes of adhesive wear. *Sci Rep*. <https://doi.org/10.1038/s41598-020-57429-5>
- Medina S, Dini D (2014) A numerical model for the deterministic analysis of adhesive rough contacts down to the nano-scale. *Int J Solids Struct* 51(14):2620–2632. <https://doi.org/10.1016/j.ijsolstr.2014.03.033>
- Persson BNJ, Albohr O, Tartaglino U, Volokitin AI, Tosatti E (2005) On the nature of surface roughness with application to contact mechanics, sealing, rubber friction and adhesion. *J Phys: Condens Matter* 17:1–62. <https://doi.org/10.1088/0953-8984/17/1/R01>. arXiv:cond-mat/0502419 [cond-mat.mtrl-sci]
- Hensel R, Moh K, Arzt E (2018) Engineering micropatterned dry adhesives: from contact theory to handling applications. *Adv Funct Mater* 28:1800865. <https://doi.org/10.1002/adfm.201800865>
- Popov V (2021) Energetic criterion for adhesion in viscoelastic contacts with non-entropic surface interaction. *Rep Mech Eng* 2(1):57–64. <https://doi.org/10.31181/rme200102057p>
- Raous M, Schryve M, Cocou M (2006) Recoverable adhesion and friction. In: Banagiotopoulos CC (ed) *Nonsmooth/nonconvex mechanics with applications in engineering*, pp 165–172. <https://hal.archives-ouvertes.fr/hal-03177510>
- Raous M (2011) Interface models coupling adhesion and friction. *C R Méc* 339(7–8):491–501. <https://doi.org/10.1016/j.crme.2011.05.007>
- Cocu M, Schryve M, Raous M (2010) A dynamic unilateral contact problem with adhesion and friction in viscoelasticity. *Z Angew Math Phys* 61:721–743. <https://doi.org/10.1007/s00033-009-0027-x>
- Allix O, Deü J-F (1997) Delayed-damage modelling for fracture prediction of laminated composites under dynamic loading. *Eng Trans* 45(1):29–46. <https://doi.org/10.24423/engtrans.680.1997>
- Courant R, Friedrichs K, Lewy H (1928) Über die partiellen differenzgleichungen der mathematischen physik. *Math Ann*. <https://doi.org/10.1007/BF01448839>

24. Moreau JJ (1988) Unilateral contact and dry friction in finite freedom dynamics. In: Moreau JJ, Panagiotopoulos PD (eds) *Non-smooth mechanics and applications*, pp 1–82. https://doi.org/10.1007/978-3-7091-2624-0_1
25. Jean M, Acary V, Monerie Y (2001) Non-smooth contact dynamics approach of cohesive materials. *Philos Trans R Soc Lond Ser A: Math Phys Eng Sci* 359(1789):2497–2518. <https://doi.org/10.1098/rsta.2001.0906>
26. Budzik MK, Wolfahrt M, Reis P, Kozłowski M, Sena-Cruz J, Papadakis L, Saleh MN, Machalicka KV, Freitas ST, Vassilopoulos AP (2021) Testing mechanical performance of adhesively bonded composite joints in engineering applications: an overview. *J Adhes*. <https://doi.org/10.1080/00218464.2021.1953479>
27. Ghanbarzadeh A, Faraji M, Neville A (2020) Deterministic normal contact of rough surfaces with adhesion using a surface integral method. *Proc R Soc A: Math Phys Eng Sci* 476(2242):20200281. <https://doi.org/10.1098/rspa.2020.0281>
28. Grierson DS, Flater EE, Carpick RW (2005) Accounting for the JKR-DMT transition in adhesion and friction measurements with atomic force microscopy. *J Adhes Sci Technol* 19(3–5):291–311. <https://doi.org/10.1163/1568561054352685>
29. Fremond M (1987) Adhesion of solids. *J Méc Théor Appl* 6(3):383–407
30. Rouleau L, Legay A, Deü J-F (2018) Interface finite elements for the modelling of constrained viscoelastic layers. *Compos Struct* 204:847–854. <https://doi.org/10.1016/j.compstruct.2018.07.126>
31. Chaboche J-L (1997) Thermodynamic formulation of constitutive equations and application to the viscoplasticity and viscoelasticity of metals and polymers. *Int J Solids Struct* 34(18):2239–2254. [https://doi.org/10.1016/S0020-7683\(96\)00162](https://doi.org/10.1016/S0020-7683(96)00162)
32. Terfaya N, Berga A, Raous M (2015) A bipotential method coupling contact, friction and adhesion. *Int Rev Mech Eng (IREME)* 9(4):341. <https://doi.org/10.15866/ireme.v9i4.5841>
33. De Saxcé G, Feng Z-Q (1998) The bipotential method: a constructive approach to design the complete contact law with friction and improved numerical algorithms. *Math Comput Model* 28(4–8):225–245. [https://doi.org/10.1016/s0895-7177\(98\)00119-8](https://doi.org/10.1016/s0895-7177(98)00119-8)
34. Carlberger T, Stigh U (2007) An explicit FE-model of impact fracture in an adhesive joint. *Eng Fract Mech* 74:2247–2262. <https://doi.org/10.1016/j.engfracmech.2006.10.016>
35. Belytschko T, Liu WK, Moran B, Elkhodary IK (2014) *Nonlinear finite elements for continua and structures*
36. Hetherington J, Askes H (2014) A mass matrix formulation for cohesive surface elements. *Theor Appl Fract Mech* 69:110–117. <https://doi.org/10.1016/j.tafmec.2013.11.011>
37. Pagani M, Reese S, Perego U (2014) Computationally efficient explicit nonlinear analyses using reduced integration-based solid-shell finite elements. *Comput Methods Appl Mech Eng* 268:141–159. <https://doi.org/10.1016/j.cma.2013.09.005>
38. Di Stasio J, Dureisseix D, Gravouil A, Georges G, Homolle T (2019) Benchmark cases for robust explicit time integrators in non-smooth transient dynamics. *Adv Model Simul Eng Sci*. <https://doi.org/10.1186/s40323-019-0126-y>
39. Moreau K, Moës N, Picart D, Stainier L (2014) Explicit dynamics with a non-local damage model using the thick level set approach. *Int J Numer Methods Eng* 102:808–838. <https://doi.org/10.1002/nme.4824>
40. Pijaudier-Cabot G, Grégoire D (2014) A review of non local continuum damage: modelling of failure? *Netw Heterog Media* 9(4):575–597. <https://doi.org/10.3934/nhm.2014.9.575>
41. Zghal J, Moës N (2021) Analysis of the delayed damage model for three one-dimensional loading scenarii. *C R Phys* 21(6):527–537. <https://doi.org/10.5802/crphys.42>